On-Site Solar Power Forecasting Using Sky-Images

Lasanthika H. Dissawa
School of Electrical, Computer & Telecommunications Engineering
University of Wollongong
Wollongong, Australia
lhddm993@uowmail.edu.au

Ashish P. Agalgaonkar
School of Electrical, Computer & Telecommunications Engineering
University of Wollongong
Wollongong, Australia
ashish@uow.edu

Duane Robinson
School of Electrical, Computer & Telecommunications Engineering
University of Wollongong
Wollongong, Australia
duane@uow.edu.au

Roshan I. Godaliyadda
Department of Electrical and Electronics Engineering
University of Peradeniya
Peradeniya, Sri Lanka
roshangodd@ee.pdn.ac.lk

Janaka B. Ekanayake
Department of Electrical and Electronics Engineering
University of Peradeniya
Peradeniya, Sri Lanka
ekanayakej@cardiff.ac.uk

Parakrama B. Ekanayake
Department of Electrical and Electronics Engineering
University of Peradeniya
Peradeniya, Sri Lanka
mpb.ekanayake@ee.pdn.ac.lk

Sarath Perera
School of Electrical, Computer and Telecommunications Engineering
University of Wollongong
Wollongong, Australia
sarath@uow.edu.au

Abstract*—The variability of solar power generation introduces significant challenges to power system operation. Accurate irradiance forecasts will help to overcome these challenges. Therefore, onsite-irradiance forecasting technique was proposed by utilizing a wide-angle camera. The proposed model predicts solar power by several minutes in advance via extracting the cloud motion vectors from sky images. Individual cloud movement was tracked by cross-correlation and motion vectors were created for each cloud. A separate model for cloud deformation and a dynamic model for cloud movement were constructed. For each cloud, cloud deformation over time was identified, and it was embedded into the cloud motion-based forecasts. To improve forecasting results, the cloud motion-based forecasts and time series forecasts were merged. The results were obtained for 1min, 2min, and 5min horizons with one-minute granularity. The MBE percentages of 11%, 10% and 12% were achieved. The effects of seasonal variations on image-based forecasting models were discussed at the end.

***Keywords*—c irradiance forecast. Solar PV forecast, sky-image, global horizontal irradiance, cross-correlation**

I. INTRODUCTION

The contribution of solar PV power generation to the electric power system has shown significant growth in recent years. However, due to PV power variability and uncertainty, the increased penetration of installed PV poses many challenges in power system planning, operation, and grid management. The impacts of intermittent nature of PV power generation on power quality, reserve planning, generating unit-commitment and scheduling occur at different time scales from seconds to days ([1], [2]).

To mitigate the effects mentioned above, several strategies were introduced such as advanced forecasting methods, maintaining flexible generation and/or load, connecting battery banks, introducing operational practices such as fast scheduling and dispatch, etc. From these approaches, solar power forecasting is the major tool used to address the risks related to high penetration of PV into the electricity grid [3].

The models used to forecast solar PV power depends on the desired time scale of the forecast. References [1] identify three forecasting horizons: intra-hour, intra-day and day ahead, which are related to grid operator activities. Intra-hour or very short-term forecasting (from a few seconds to minutes) can be used for ramp up/down event predictions, PV and storage control and it can be used for electricity market operations, such as the Australian electricity market which uses 5 minute PV forecasts [4], [5]. Further, in the smart grid environment, very short-term forecasting of solar PV can be used for smart inverter and smart meter applications.

The power generated by PV arrays mainly depends on two weather elements: type and amount of clouds in the PV site, and the ambient temperature of the site. The number of clouds and the type of cloud affects the solar irradiance that reaches the ground since clouds attenuate, reflect, and scatter the irradiance coming from the sun before it reaches the ground. Therefore, it directly affects PV plant output. When considering the rate of change temperature and irradiance with time, the rate of changes of temperature is usually not significant for the small-time window, and it gradually changes with time. But the solar irradiance can change rapidly within a very short period. Therefore, in short-term PV power forecasts, the PV power changes due to temperature can be neglected. So, the ability to perform accurate forecast on surface solar irradiance can provide an accurate PV power forecast.

According to the three-forecasting time horizons; intra-hour, intra-day, and day ahead, the input data used in the irradiance and PV power forecasting models vary. Numerical Weather Prediction (NWP) models-based irradiance forecasting methods can give accurate predictions in the range of 6 hours to several days. While in a time horizon less than 6 hours, satellite data-based models typically outperform NWP models [6]. Using satellite images, the prediction is made for the temporal range from 30 minutes up to 6 hours due to time and space availability [6]. For the intra-hour range predictions, cloud information from ground-based sky images, or/and time-series models [7]–[9] which based on historical data are employed.

NWP models and Satellite cloud observation data-based forecast models are inadequate to achieve high temporal and spatial resolution for intra-hour irradiance forecasts. Sky observations using a ground-based sky camera system makes it possible to fill the forecasting gap, and it can deliver short-term, more precise area-specific irradiance forecasts[8]–[11].

In cloud motion estimation-based irradiance forecasting models, mainly two algorithms were used to find the cloud motion vectors across the image; Cross-Correlation (CC) algorithm and optical flow algorithms such as Lucas-Kanade optical flow algorithm and variational optical flow algorithm.

References [12], [13] use CC algorithm to estimate block movement and [8], [9], [14], [15] use optical flow-based cloud feature point tracking algorithm to estimate the cloud boundary feature point movement.

In CC based cloud motion tracking methods, before applying CC, the sky image is partitioned into subsets of pixels of equal size without considering the individual clouds or cloudy regions. Then CC is applied to each block, and block movement was estimated. In [13] and [14] spatial homogeneity of cloud velocity is assumed, and the vector field obtained through the CC is further processed, and a weighted average cloud velocity across the image is found. After that, the average cloud velocity is defined as the representative of the velocity of all clouds in the image. Then a footprint of the cloud shadows on the ground is created using a binary cloud image, and it is moved according to the estimated cloud moving velocity. Then using the estimated clear sky irradiance values and shadow movement, the irradiance is forecasted. This block-wise cloud movement estimation will work for a single cloud layer (moving in one direction), but for multi-layer (clouds move in different directions) cloudy sky, this may result in inaccurate irradiance forecasts. The other problem with this method is the homogeneous area of the image (e.g. on a large white cloud) may often lead to abnormal vectors. Therefore, instead of using an average moving velocity for all clouds, the block-wise movement estimation method is modified in [13] to obtained single-layer/multi-layer cloud motion vectors. However, here, the irradiance prediction is not made directly using the cloud motion estimation. The cloud estimation result is only applied to find present image cloudiness using a pixel's red-blue value ratio. In here, it was assumed that the value at a one-time instance depends only on the immediately preceding step. Hence the method may be susceptible to sudden fluctuations, and the actual dynamic model for cloud movement has not been constructed.

References [17], [15] propose cloud tracking and irradiance forecasting method based on the Lucas-Kanade optical flow algorithm. In these studies, it was assumed that the movement of the cloud is small between two image frames, and the image pixel values do not change over the consecutive frames. The method described in [16] predicts the trajectory of the selected cloud feature points in the image sequence. Using the cloud trajectories, it determines the time duration for clouds to reach a known area in the image whereas the reference [17] uses shadow mapping method as in [16], [12]. But in [18], the traditional Optical Flow (OF) estimation method is adopted to define the motion vector from one frame to the next frame by assuming consistent brightness. Here local cloud tracking is utilised, and multiple cloud layers are identified.

The primary limitation of the sky image-based cloud movement and irradiance prediction reported in the literature is the lack of incorporating the information of cloud deformation. As the cloud itself is not a rigid body, cloud shape changes throughout time is an essential consideration for prediction algorithms. On top of that in certain methods the overall movement flow of each cloud in the sky view image is not taken into consideration hence for example in many of them, one of the primary deficiencies is that the entire sky image particles are assumed to be going at a uniform velocity throughout the image without considering the relative movements between clouds. However, practically, this is not the case, and this method may lead to errors in the results. To track the movement of the clouds over many image frames and to cover a large area of the sky, the wide-angle camera lens is used in most of the methods. However, the wide-angle lenses introduce different image distortions such as fisheye lens distortion. To mitigate these effects, the images were undistorted. As a result of the distortion removal process, the cloud's shape changed noticeably frame to frame. This may create errors in some optical flow-based PV forecasting methods since it assumes the movement of the cloud is small between two image frames, and the image pixel values do not change over the consecutive frames.

This paper introduces a cloud movement estimation-based onsite solar power forecasting model using an inexpensive fisheye-lens camera to forecast PV ramp-up down events several minutes in advance. The overall cloud movement prediction depends on the fusion of the dynamic and deformation models to give a more reliable estimate of the cloud movement. Once the motion of the cloud is predicted as a whole body, it determines accurate time instances of occlusion of the sun (time takes by a cloud to reach the sun and pass the sun) thus enabling to identify ramp down events few minutes in advance. Further, various sky states such as clear sky, partially cloudy sky and cloudy sky were defined considering the ratio of the cloudy pixel in the image. This classification was used for the accurate prediction of power from the dynamic model constructed. On top of that, time-series predictions were incorporated into the model to capture the power drops occur due to fast-moving clouds. Rather than just incorporating the historical data for the forecast, a fusion of cloud tracking model with the time series forecasts enhances the power forecast results.

This paper is organised as follows. Section II gives the details of the inexpensive ground-based sky imager, cloud detection method, details of cloud movement tracking algorithm, PV power forecasting model and error calculation. The experimental results and subsequent analyses are described in Section III, followed by conclusions in Section IV.

II. Materials and Method

A. Data

Clouds are the primary cause of the variability of solar PV output power. When the clouds come in between the sun and the PV panel, the cloud blocks the radiation coming from the sun to the PV panel. It results in sudden, rapid changes in PV power output, which is called a 'ramp event'. The fluctuations last until the cloud moves away from the sun-PV panel path.

To forecast the short-term PV power, the local cloud motion details were important to incorporate into the PV power forecasting systems as the short-term fluctuations mainly occurred due to the clouds above the PV site. According to the cloud motion details and the current cloud position and cloud size, the future position of the cloud shadow and the deformation of the cloud shadow were predicted. Hence, the PV plant power output was estimated.

For the experiment, since the sky condition varies from time to time, and the variation is area-specific, the sky images were captured near to two different PV plants using inexpensive, high-resolution USB fisheye-lens cameras. The cameras have a wide-angle lens (ELP-USB500W05G-L 170) and are connected to mini PCs. Since the cameras are placed

in the field, the white balance property in cameras was set to get a clear sky image on a sunny environment using a Matlab script. Further, the image capturing frequency was also set using the same Matlab script.

Two cameras were installed at two locations. One is in the Faculty of Engineering, University of Peradeniya, Sri Lanka and at the other camera is placed in the Sustainable Buildings Research Centre (SBRC), University of Wollongong, Australia. The images were captured every 10 seconds and were stored in JPEG format, which has a resolution of 1024x768 pixels.

The other input information required is the power measurement or irradiance measurement on the site. PV power data and irradiance data were obtained from a 55kW horizontal rooftop PV system installed at the Department of Electrical and Electronics Engineering, University of Peradeniya, Sri Lanka, and from a 20kW horizontal rooftop PV system and from the weather station installed at the SBRC, University of Wollongong. The camera and the weather-station are fixed near to the PV system. The power measurements and irradiance measurements are stored in a 1-minute interval.

B. Method

Fig. 1 shows the basic flow diagram of the forecasting model implemented in this paper. First, the clouds were separately identified from sky images. Then according to the percentage of cloud pixels in the image, the sky condition is identified as sunny, overcast or partially cloudy. Identification of the sky condition is important as the motion of the cloud tracking is only applicable for partially cloudy sky condition.

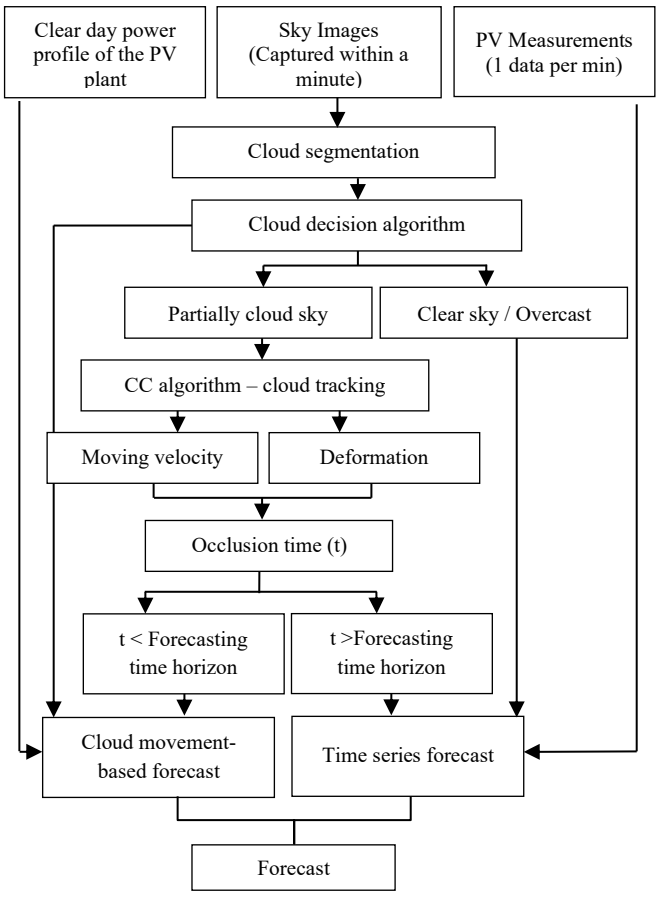

Fig. 1 PV forecasting methodology

After that, cloud motion tracking and irradiance drop forecasting were done.

1) Cloud Segmentation

Initially, the images taken were cropped into 690 x 690 pixels size image to remove the unwanted area from the image. Then, the fish-eye lens distortion from the raw image was removed using Matlab 'undistortImage' function as the fisheye introduces nonlinearities near the edge of the image. Fish-eye lens distortion correction process transforms the distorted fisheye images back to the natural-looking view. Fig. 2 shows the raw image and the undistorted image.

a *b* *c*

Fig. 2 (a) Raw image, (b) distortion removed image and (c) image mask

The whole sky image visually represents the sky (clouds and the sun) and unwanted surrounding objects such as buildings, trees etc. Therefore, the unwanted components in the image were removed. For this, the difference between red, green, and blue (RGB) components of the unwanted parts in the sky area were identified and by applying threshold values to RGB components in the image, the unwanted components were separately identified, and a mask was created accordingly. It is shown in Fig. 2(c).

Next step is to identify clouds separately from the blue sky. Obtaining a correct binary image which includes only the clouds is needed to track the movement of the individual cloud. A blue sky detection method was implemented by incorporating YCbCr (luminance (Y) and chrominance (Cb and Cr are the blue-difference and red-difference chroma components)) [19] properties of the image with the red to blue ratio (RBR) values. The blue-sky area in the RGB image was identified, and the sky binary image was obtained. After that, a median filter was applied to the binary sky image to smooth the gagged edges around the boundaries. Further, the small (no of pixels belongs to a cloud < 5000) white patches (< 1% area) were removed from the binary image and other white patches were selected for the cloud tracking algorithm. In the binary image, clouds and the sun area are represented by white colour and clear sky by black. To track the clouds separately, the individual white patches were identified separately by the connected component analysis, as shown in Fig. 3 (a).

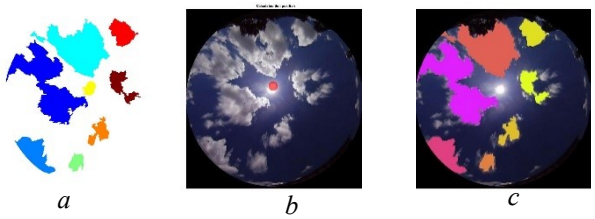

a *b* *c*

Fig. 3 (a) separately identified white patches (b) detected the position of the sun and (c) identified cloud area marked on the image

Finding the location of the sun on the image is important to identify the cloud patches in the sky image and to select the clouds moving toward the location of the sun to calculate the time for occlusion for these clouds. According to the date and time, the position of the sun on the sky image was found using the zenith angle, azimuth angle, camera orientation, and using

the camera mapping function. The [*X, Y*] coordinates of the sun's centre position on the distorted image were calculated, and hence, the corresponding region of the sun on the distorted image was identified. Fig. 3(b) shows the location of the sun on the image in the red colour. Then, using the centre coordinates of the sun, the connected component which related to the sun's centre position was identified as the region belongs to the sun. The other connected components were considered as individual clouds Fig. 3(c).

2) Cloud Decision Algorithm

In the forecasting algorithm, consecutive image frames captured within a minute were selected for one iteration to do a few minutes ahead cloud motion predictions. The binary conversion of the first image frame in the image sequence was classified as sunny, overcast or partially cloudy according to the percentage of the white pixel ("*WP*") in the binary sky image. The sky state was identified at the beginning of each iteration. According to the white pixel percentage, three categories were defined as in Table 1. By comparing the power measurements and the white pixel percentage, the boundaries 20% and 80% were selected to categories the image into three categories as given in Table 1.

TABLE 1 ASSIGNING SKY STATE - SUNNY, OVERCAST AND PARTIALLY CLOUDY

Sky State	Sunny	Overcast	Partially Cloudy
Limits	<20% WP	>80% WP	20%-80% WP

Once the initial image is classified into the partially cloudy condition, the normalized cross-correlation based cloud motion tracking algorithm was applied to each cloud boundary segments, and the time for occlusion was found. According to the calculated time, PV power fluctuations were forecasted. Fig. 4 shows three consecutive image frames obtained for sunny, partially cloudy and overcast sky conditions.

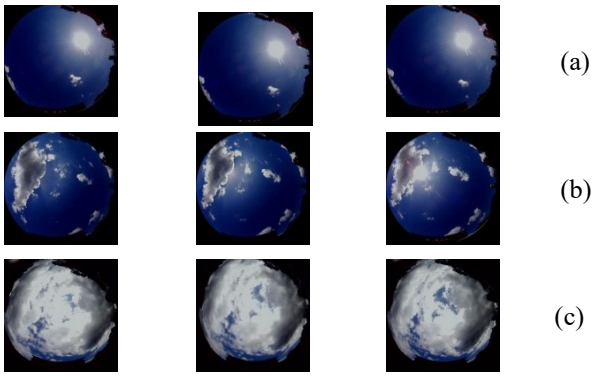

Fig. 4. Images of three different sky conditions obtained on 4th July 2017 ((a) Sunny, (b) partially cloudy and (c) overcast)

3) Cloud Boundary Tracking Algorithm

To track the movement of clouds from one image frame to the next image frame, the normalized cross-correlation (CC) algorithm was applied to each cloud boundary segment. Normalized cross-correlation is commonly used as a metric to evaluate the amount of similarity between two images.

The first step in the cloud movement tracking method is to select boundary points [x_1, y_1] around each cloud on the first image frame. The boundary points were obtained from the binary sky image. The number of boundary points around each cloud depends on the cloud size and at least 25 boundary points were selected.

The next step is to detect the corresponding points of the selected [x_1, y_1] points on the second image frame. For this, the normalised CC method was applied to boundary segments around each boundary point. To apply the CC, the images were converted into grayscale considering the green component of the RGB image. A region of 40 x 40 pixels around a boundary point [x_1, y_1] in frame1 was selected as the template image. Then, in the next image frame, a region of 60 x 60 pixels around the same location was selected as the search window. These two block sizes were chosen considering average wind speed and comparing motion vectors of adjacent image frames for different block sizes. After that, the template image was correlated with the next image frame's searching window. The location of the highest correlation was identified. Template size was selected according to the pixel difference between selected two boundary points such that the template size is smaller than the difference between selected two boundary points. Further, the search window size was selected by assuming that the selected point does not move beyond 20 pixels from its initial position within 10 seconds. This size was obtained by testing several image frames obtained on different days.

Fig. 5 shows the template image around a boundary point, the cross-correlation output and the search window with the tracked boundary segment. The size of the search window in the next image frame is small (0.75% of full sky image) compared to the cloud size (> 1%). Therefore, the highest correlation point was assumed as the corresponding boundary point in the next image frame, and by considering the highest correlation point, the boundary segment motion vector was defined. Fig. 6 shows tracked boundary segments (red) from frame f, to frame f+4, and it shows the boundary point trajectories over a minute.

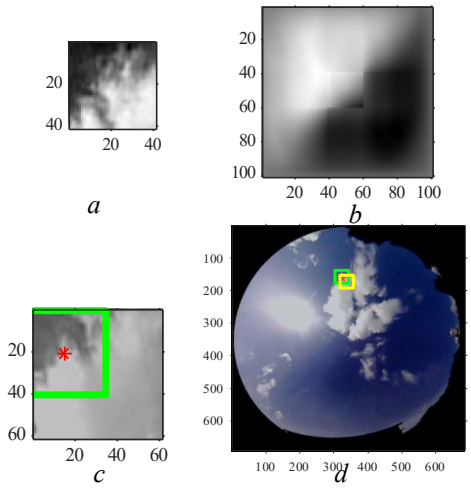

Fig. 5. (a) Template image to search for, (b) correlation output, (c) selected searching window in 2nd image frame with correlation result (inside the green square) and (d) the 2nd image frame with the position of 1st image cloud boundary segment (yellow) and position of 2nd image frame tracked boundary segment (green)

4) Cloud Deformation

The shape of the cloud changes with time even if they are not moving. The clouds like Cumulus, form and dissipate with the time according to the environmental conditions. If a forming cloud does not move, the average cloud moving velocity becomes zero. In this scenario, the cloud size increases with the time and shadow will appear on the PV plant. Therefore, it is necessary to identify cloud deformation

estimation into the PV forecasting model. From the tracked feature point details, deformation of the cloud was found.

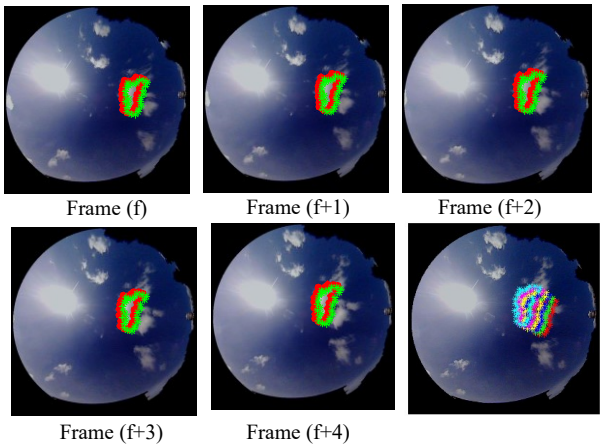

Fig. 6 Tracked boundary segments (red) from frame (f to f+4), trajectories over a one iteration (5 image frames)

The segmented clouds were selected separately and then for each frame; the tracked boundary segments were arranged with respect to the centroid coordinates of the cloud on the initial image frame. Then, position arrays were created for each boundary point considering their new coordinates. Fig. 7 shows the tracked cloud over a single iteration and the same cloud after arranging the tracked cloud boundaries with respect to the centroid "*C*" of the initial position of the cloud.

Using the position arrays of boundary points, for each point, the ΔX and ΔY coefficients for each boundary point were estimated using the position arrays via (1) and (2). Then, according to the calculated parameters, future cloud coordinates were obtained using (3) and (4).

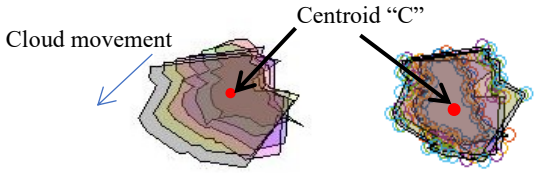

Fig. 7 Cloud movement over 1 min, (c) cloud shape with respect to initial image cloud's centroid

$$\Delta X = \frac{1}{N-1}\sum_{i=2}^{N} X_i - X_{i-1} \quad (1)$$

$$\Delta Y = \frac{1}{N-1}\sum_{i=2}^{N} Y_i - Y_{i-1} \quad (2)$$

$$X' = X_N + \Delta X + x_c \quad (3)$$

$$Y' = Y_N + \Delta Y + y_c \quad (4)$$

If "*P*" is the selected boundary point. Tracking coordinates of point "*P"* from frame 1 to 6 is $[x_i,y_i]$, where i=1 to N (N = 6). Coordinates of the centroid "C" of the cloud on frame 1 is $[x_c,y_c]$ and new coordinates with respect to C, is denoted by $[X_i, Y_i]= [x_i-x_c,y_i-y_c]$, where i=1 to N.

5) Time for Sun Occlusion

Using the movement of each point from the first frame to the last frame, the motion velocities of each point was calculated. After that, the clouds move in the direction of the location of the sun was identified. Since the camera was placed near to the PV plant, the image area, which creates a shadow on the PV plant, will be the location of the sun on the sky image. If a cloud moves towards the location of the sun on the image, then a shadow will place on the PV plant. Based on that, future irradiance drop was estimated.

For the clouds which move towards the location of the sun (on the image), the estimated cloud boundary points (x',y') were moved according to their respective average cloud moving velocities. The points move in the direction of the location of the sun (angle $|\alpha|<15$ degrees) (α is the angle between the motion vector of feature point ("*P*") and the line which is drawn from point "*P*" to the centroid of the sun were selected and time to reach the location of the sun was calculated. If it passes the location of the sun, the time to pass the location was calculated. The mean time for each cloud to pass the sun was calculated, and it was taken as the maximum time for clouds to pass the sun. Then, the minimum time was selected, and it was defined as the starting time to cover the sun (ramp down event).

6) Hybrid Forecasting Model

By combing the time series forecasts with the cloud motion-based forecasts, the final solar power forecasting results were obtained. Based on the results coming from the cloud decision algorithm (clear, overcast or partially cloudy condition), if the image is in the overcast or clear sky state, then the time series model was used to forecast the power. On the other hand, if the image is categorized into a partially cloudy condition, the cloud motion-based forecasting model was used. But if the time for occlusion time is higher than the forecasting time horizon, again the time series model was used for the forecast.

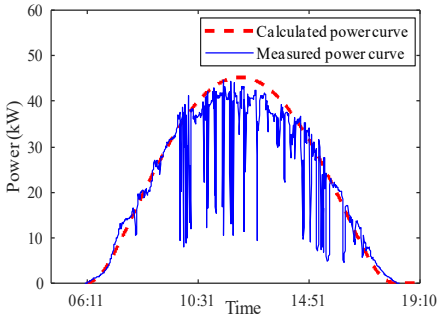

Fig. 8 Measured PV power (blue) and mathematically obtained power curve (red) using Hottel's Clear Day model (Peradeniya)

The irradiance drop factor was found using the irradiance measurements obtained from partially cloudy days. The irradiance drop percentage was found using the mathematically calculated clear sky Global Horizontal Irradiance (GHI) values. The average percentage irradiance drop is about 35% of clear day GHI value. If the cloud is going to cover the sun within the forecasting time horizon (1 min, 2 min or 5 min), it was assumed that the predicted power is 35% of clear day power value. The power forecast was calculated by multiplying the clear day power value by a factor of 0.35.

Clear day power profile was obtained using the mathematical irradiance curve. To create the mathematical irradiance curve for Peradeniya (7.27° N, 80.59° E), Hottel's Clear Day model [20] was utilized, on the other hand, to create the mathematical irradiance curve for Wollongong (34.40° S, 150.88° E), ASHRAE model [21] was used.

Then using PV plant area, PV module efficiency and performance ratio of the panel, the generated PV power on a sunny day was obtained using the mathematically calculated Global Horizontal Irradiance ("*GHI"*) as in (5).

$$PV\ Power = GHI \times A \times \epsilon \times PR \quad (5)$$

where, "A" is the area of the panel in m^2, "ϵ" efficiency and "GHI" global horizontal irradiance on the panel area and "PR" performance ratio of the panel.

The measured PV power (blue) and mathematically obtained power curve (red) using Hottel's Clear Day model is shown in Fig. 8.

Using the past PV power measurements, time series forecast was obtained. Using the average of the measured 1 min power values obtained during previous forecasting time horizon "Δ_{ft}", future power values were forecasted as in the equation (6).

$$P_{ft_n} = \frac{\sum_{T=t}^{T=tn-1} P_{mT}}{\Delta_{ft}} \quad (6)$$

where P_{ft_n} is the power forecast for time t_n , P_{mT} is the measured power at time T and Δ_{ft} is the forecasting time horizon .

III. RESULTS

A. Data

The PV power forecasting results were obtained from 9.30 am to 3.30 pm with 1 min granularity for 10 days. Therefore, 360 (60 min × 6 h) forecasting results were obtained for each day. Selected 10 days were partially cloudy days. Sunny and overcast days were neglected.

The data collected from two different locations were used to test the forecasting model. Selected two locations are completely geographically different and have different climatic conditions. One location is in Peradeniya, Sri Lanka which is closer to the Equator and has a mountainous environment, on the other hand, the other location is in Wollongong, Australia which is located between Tropic of Capricorn and the Antarctic Circle and lies on the narrow coastal strip. In Wollongong, seasonal variations due to the change of the path of the sun can be seen significantly than in Peradeniya. Therefore, few days in winter season and spring season were chosen to collect data from Wollongong area.

To evaluate the effects of the path of the sun and the cloud moving direction in the image based forecasts, the average wind direction and average wind speed data were obtained from a freely available weather database [22]. For the selected days in Wollongong area, the wind velocity data are given in Table 2.

B. Performance metrics

To evaluate the forecasting model, the forecasting errors were calculated. The Root Mean Square Error (RMSE) and Mean Absolute Error (MAE) between the forecasted power and measured power [23] were calculated using equations (12) and (13) for different forecasting time horizons as in [24].

$$RMSE_c = \sqrt{\frac{1}{T}\sum_t \left(P_m(t) - P_f(t)\right)^2} \quad (12)$$

$$MAE_c = \frac{1}{T}\sum_t \left|P_m(t) - P_f(t)\right| \quad (13)$$

where, $P_m\ (t)$ is the measured PV power, and $Pf\ (t)$ is the forecasted PV power at time t for the forecasting time horizon 'c'. 'T' is the sum of overall time samples used in the evaluation per day (360 time samples).

To compare the forecast performance, the skill factor (SF) was calculated [24]. The skill factor of the forecast data compares our forecast with a persistence method. The persistence method used here is defined as the power on the day 'd+1' equals to power on day 'd'. The skill factor was calculated using equation (14); where, RMSEp, is the root mean square error of persistence method and RMSEc is the root mean square error of our method. For each forecasting time horizon, SF was calculated.

$$SF = 1 - \frac{\mathrm{RMSE_c}}{\mathrm{RMSE_p}} \quad (14)$$

If the SF value is greater than zero, it implies that the proposed forecast outperforms the persistence method.

TABLE 2 : AVERAGE WIND DIRECTION FOR THE SELECTED DAYS IN WOLLONGONG ACCORDING TO [22].

Date	Time	Average Wind direction (coming from)	Avg. Wind Speed /(km/h)
July 4, 2018 (Winter)	***6.00am to 12.00 pm,***	North -Northwest	20
	12.00 pm to 6.00pm	North-Northeast	21
July 9, 2018 (Winter)	***6.00am to 12.00***	West	20
	12.00 pm to 6.00pm	South	23
Sep 15, 2018 (Spring)	***6.00am to 12.00***	Northeast	17
	12.00 pm to 6.00pm	Northwest	33
Sep. 19, 2018 (Spring)	***6.00am to 12.00***	North-Northwest,	24
	12.00 pm to 6.00pm	West-Northwest	33
Sep. 20, 2018 (Spring)	***6.00am to 12.00***	Southwest	23
	12.00 pm to 6.00pm	South-Southeast	21
Sep 23, 2018 (Spring)	***6.00am to 12.00***	South	23
	12.00 pm to 6.00pm	South	24
Oct. 11, 2018 (Spring)	***6.00am to 12.00***	South-Southwest	23
	12.00 pm to 6.00pm	South -Southeast	30

C. Forecasting results and discussion

The results were generated for three forecasting time horizons; 1 min, 2 min and 5 min with one-minute granularity. Fig. 9 a) and b) show a comparison between measured power values and forecasting results in 1 min and 5 min forecasting time horizons respectively.

Table 3 shows the calculated errors for the selected 10 days and it compares the results for three forecasting time horizons for two different locations. From 1 min, 2 min and 5 min forecasting results, MAE is higher in 5 min forecasting time interval in results obtained from Peradeniya. Considering average percentage of RMSE, 1 min and 2 min time interval show a low error percentage at both locations. According to the forecasting errors of different forecasting time horizons, most of the time, skill factor remains positive for 2 min and 5 min forecasting time intervals. Therefore, the hybrid forecasting model introduced in this paper is more accurate than the persistent model which uses the previous day measurements as forecasts.

Considering the forecasting location as Wollongong, during the winter season, the path of the sun goes near to the image boundary (the sun has a large Zenith angle) as in Fig.10. Therefore, it is only possible to capture the clouds coming from one part of the sky image. In this case clouds coming from North, Northwest and Northeast cannot be tracked.

The average direction of the wind on 4th July 2018 was from North-Northwest and North-Northeast. Therefore, most

irradiance drop scenarios were not captured. This resulted in increase of errors in the forecasting results on 4th July 2018. Further, on 9th July 2018 (another day in winter season), the average wind direction was from West and South. Thus, the clouds moving from those directions can be tracked. Therefore, the forecasting error on 9th July 2018 is less than as of 4th July 2018.

TABLE 3 FORECASTING ERRORS AND SKILL FACTORS FOR DIFFERENT FORECASTING TIME HORIZONS IN TWO LOCATIONS

Location	Day	Time horizon	RMSE (kW)	RMSE %	MAE (kW)	SF
UoP 55kW system	*July 3, 2017*	*1min*	10.14	18.44	6.17	0.44
		2min	9.02	16.4	5.06	0.5
		5min	11.67	21.22	7.64	0.35
	July 4, 2017	*1min*	12.89	23.44	8.33	0.29
		2min	11.99	21.80	6.93	0.34
		5min	13.87	25.22	9.35	0.24
	July 5, 2017	*1min*	10.14	18.44	6.17	0.44
		2min	9.02	16.4	5.06	0.5
		5min	11.67	21.22	7.64	0.35
UoW 20kW system	*July 4, 2018 (Winter)*	*1min*	13.0	65.00	10.02	0.02
		2min	15.13	75.65	11.16	-0.12
		5min	17.64	88.20	13.87	-0.3
	July 9, 2018 (Winter)	*1min*	2.13	10.65	1.01	-0.77
		2min	0.97	4.85	0.45	0.19
		5min	0.95	4.75	0.45	0.21
	September 15, 2018 (Spring)	*1min*	2.42	12.10	1.26	-0.03
		2min	2.11	10.55	1.31	0.10
		5min	1.80	9.00	0.97	0.23
	September 19, 2018 (Spring)	*1min*	3.57	17.85	2.26	-0.08
		2min	3.26	16.3	2.00	0.02
		5min	3.16	15.8	1.98	0.05
	September 20, 2018 (Spring)	*1min*	3.47	17.35	1.95	-0.65
		2min	2.07	10.35	1.17	0.01
		5min	2.57	12.85	1.36	-0.22
	September 23, 2018 (Spring)	*1min*	4.48	22.40	2.78	-0.19
		2min	3.11	15.55	1.92	0.18
		5min	3.14	15.70	1.91	0.17
	October 11, 2018 (Spring)	*1min*	3.40	17.00	2.27	0.55
		2min	6.62	33.10	5.06	0.11
		5min	6.63	33.15	5.07	0.11

Table 4 shows the average of RMSE percentage and MAE percentage at both locations (the error result on 4th July 2018 at Wollongong is excluded). Overall, 1 min, 2 min and 5 min forecasting results have 18.2%, 16.7% and 18.8% averages of RMSEs' and 11.1%, 10.1% and 12.4% averages of MBEs', respectively. In all three forecasting time horizons, the average SF remains positive. Therefore, most of the time, the method introduced in this paper performs better than the persistent model.

TABLE 4. AVERAGE RMSE% AND MAE% (WITHOUT THE RESULTS ON 4TH JULY 2018 (WOLLONGONG))

Location	Time interval	Average (RMSE %)	Average (MAE %)
Peradeniya	1 min	20.1	12.5
	2 min	18.2	10.3
	5 min	22.6	14.9
Wollongong	1 min	16.23	9.6
	2 min	15.12	9.9
	5 min	15.21	9.8

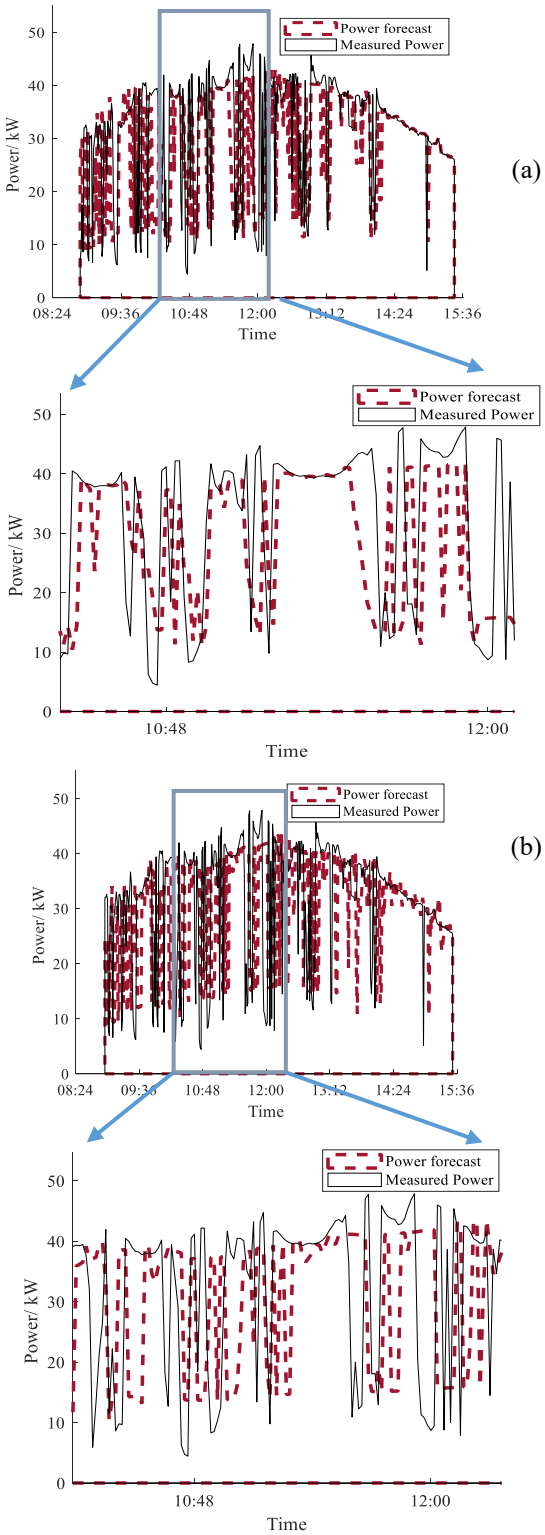

Fig. 9 a) 1 min and b) 5min ahead forecast on July 4, 2017

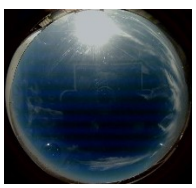

2018/07/04 12.00

Fig.10 Location of the sun on a winter day at 12.00 pm

IV. CONCLUSIONS

A hybrid model for solar power forecasting based on cloud motion tracking with time series forecasting was introduced. The method was implemented using ground-based whole sky images. The method was tested for two different locations and errors were calculated.

This local cloud observation-based PV forecasting model was implemented using inexpensive cameras. The sky imager gives an idea about real-time sky cloud condition above the PV plant, and the wide-angle lens enables to grab the large area of the sky into the image. It increases the forecasting time horizon since the cloud can track for a long time. The new cloud segmentation method can identify white clouds as well as grey clouds by applying thresholds to YCbCr image. Further, this cloud identification method does not require any training phase as in some methods but need to identify correct threshold values.

The cloud deformation estimation is essential when the clouds are formed suddenly without moving fast. Therefore, the method implemented in this paper incorporates the cloud deformation estimations to the forecasting model. The time series-based forecasting model fails to forecast the PV drops before it happens. On the other hand, only using the cloud motion-based forecasting model, power drops due to fast-moving clouds, the drops occur when the sun is near to the boundary and when the clouds are coming from a direction which the clouds cannot be tracked the power drops cannot be identified. Further, when the sky is sunny or overcast, the PV profile does not look the same as the mathematical curve. Therefore, to mitigate these problems, a fused model was introduced. For the 1minute forecasting horizon, PV drops were identified before it occurs using this model.

Since most of the time skill factor remains positive for 2 min and 5 min time interval, the hybrid forecasting model introduced in this paper is more accurate than the persistent mode. From this forecasting model, the average RMSE percentage achieved for the selected days are 18.1%, 16.7% and 18.9% for 1 min, 2 min and 5 min ahead forecasts, respectively. Further, the average SF remains positive for all three forecasting time horizons.

When implementing this on an area like Wollongong, during the winter season, the path of the sun goes near to the image boundary (the sun has a large Zenith angle). Therefore, it is only possible to capture the clouds coming from one part of the sky image. Hence, some irradiance drop scenarios cannot be captured. This may increase the errors in the forecasting results. In this scenario, the time series forecasting part of the model introduced in this paper will dominate in the forecasting model.

Sky image-based forecasting models have some difficulties of identifying the drop percentage, as the thickness of the clouds is not uniformly distributed. Some parts of the cloud may enhance the irradiance which results in an increase in the power output instead of drop. On the other hand, most of the times; clouds create sudden huge irradiance drops. Therefore, one moving cloud may not create single PV drop until it passes the PV location, but creates PV fluctuations (drops and rises) due to its non-uniformity. This may generate unexpected fluctuations compared to the forecasted results. As a conclusion, this hybrid PV forecasting model enables to identify ramp down events, a few minutes in advance with high accuracy.

REFERENCES

[1] L. Bird, M. Milligan, and D. Lew, 'Integrating variable renewable energy: Challenges and solutions', *Natl. Renew. Energy Lab.*, 2013, Accessed: Aug. 17, 2016. [Online]. Available: http://www.nrel.gov/docs/fy13osti/60451.pdf.

[2] C. Wan, J. Zhao, Y. Song, Z. Xu, J. Lin, and Z. Hu, 'Photovoltaic and solar power forecasting for smart grid energy management', *CSEE J. Power Energy Syst.*, vol. 1, no. 4, pp. 38–46, Dec. 2015, doi: 10.17775/CSEEJPES.2015.00046.

[3] K. D. Orwig *et al.*, 'Recent Trends in Variable Generation Forecasting and Its Value to the Power System', *IEEE Trans. Sustain. Energy*, vol. 6, no. 3, pp. 924–933, Jul. 2015, doi: 10.1109/TSTE.2014.2366118.

[4] X. Ai *et al.*, 'Multi-time-scale coordinated ramp-rate control for photovoltaic plants and battery energy storage', *IET Renew. Power Gener.*, vol. 12, no. 12, pp. 1390–1397, 2018, doi: 10.1049/iet-rpg.2018.5190.

[5] 'Australian Energy Market Operator', *Australian Energy Market Operator*, Sep. 17, 2013. http://www.aemo.com.au/ (accessed Apr. 06, 2018).

[6] H. M. Diagne, P. Lauret, and M. David, 'Solar irradiation forecasting: state-of-the-art and proposition for future developments for small-scale insular grids', 2012, Accessed: Jun. 10, 2016. [Online]. Available: https://hal.archives-ouvertes.fr/hal-00918150/.

[7] M. N. Akhter, S. Mekhilef, H. Mokhlis, and N. M. Shah, 'Review on forecasting of photovoltaic power generation based on machine learning and metaheuristic techniques', *IET Renew. Power Gener.*, vol. 13, no. 7, pp. 1009–1023, Feb. 2019, doi: 10.1049/iet-rpg.2018.5649.

[8] D. Bernecker, C. Riess, E. Angelopoulou, and J. Hornegger, 'Continuous short-term irradiance forecasts using sky images', *Sol. Energy*, vol. 110, pp. 303–315, Dec. 2014, doi: 10.1016/j.solener.2014.09.005.

[9] C. W. Chow, S. Belongie, and J. Kleissl, 'Cloud motion and stability estimation for intra-hour solar forecasting', *Sol. Energy*, vol. 115, pp. 645–655, May 2015, doi: 10.1016/j.solener.2015.03.030.

[10] C.-L. Fu and H.-Y. Cheng, 'Predicting solar irradiance with all-sky image features via regression', *Sol. Energy*, vol. 97, pp. 537–550, Nov. 2013, doi: 10.1016/j.solener.2013.09.016.

[11] J. Alonso-Montesinos, F. J. Batlles, and C. Portillo, 'Solar irradiance forecasting at one-minute intervals for different sky conditions using sky camera images', *Energy Convers. Manag.*, vol. 105, pp. 1166–1177, Nov. 2015, doi: 10.1016/j.enconman.2015.09.001.

[12] K. Stefferud, J. Kleissl, and J. Schoene, 'Solar forecasting and variability analyses using sky camera cloud detection & motion vectors', in *2012 IEEE Power and Energy Society General Meeting*, 2012, pp. 1–6, Accessed: Aug. 17, 2016. [Online]. Available: http://ieeexplore.ieee.org/xpls/abs_all.jsp?arnumber=6345434.

[13] H. Huang *et al.*, 'Cloud motion estimation for short term solar irradiation prediction', in *Smart Grid Communications (SmartGridComm), 2013 IEEE International Conference on*, 2013, pp. 696–701, Accessed: Jun. 10, 2016. [Online]. Available: http://ieeexplore.ieee.org/xpls/abs_all.jsp?arnumber=6688040.

[14] M. Cervantes, H. Krishnaswami, W. Richardson, and R. Vega, 'Utilization of Low Cost, Sky-Imaging Technology for Irradiance Forecasting of Distributed Solar Generation', in *2016 IEEE Green Technologies Conference (GreenTech)*, Apr. 2016, pp. 142–146, doi: 10.1109/GreenTech.2016.33.

[15] W. Richardson, H. Krishnaswami, R. Vega, and M. Cervantes, 'A Low Cost, Edge Computing, All-Sky Imager for Cloud Tracking and Intra-Hour Irradiance Forecasting', *Sustainability*, vol. 9, no. 4, p. 482, Mar. 2017, doi: 10.3390/su9040482.

[16] C. W. Chow *et al.*, 'Intra-hour forecasting with a total sky imager at the UC San Diego solar energy testbed', *Sol. Energy*, vol. 85, no. 11, pp. 2881–2893, Nov. 2011, doi: 10.1016/j.solener.2011.08.025.

[17] P. Wood-Bradley, J. Zapata, and J. Pye, 'Cloud tracking with optical flow for short-term solar forecasting', 2012, Accessed: Apr. 06, 2018. [Online]. Available: https://openresearch-repository.anu.edu.au/handle/1885/28800.

[18] Z. Peng, D. Yu, D. Huang, J. Heiser, S. Yoo, and P. Kalb, '3D cloud detection and tracking system for solar forecast using multiple sky imagers', *Sol. Energy*, vol. 118, pp. 496–519, Aug. 2015, doi: 10.1016/j.solener.2015.05.037.

[19] K. Jack, *Video Demystified: A Handbook for the Digital Engineer*, 5 edition. Newnes, 2011.

[20] H. C. Hottel, 'A simple model for estimating the transmittance of direct solar radiation through clear atmospheres', *Sol. Energy*, vol. 18, no. 2, pp. 129–134, Jan. 1976, doi: 10.1016/0038-092X(76)90045-1.

[21] M. J. Ahmad and G. N. Tiwari, 'Solar radiation models—A review', *Int. J. Energy Res.*, vol. 35, no. 4, pp. 271–290, doi: 10.1002/er.1690.

[22] 'Weather in July 2018 in Wollongong, New South Wales, Australia'. https://www.timeanddate.com/weather/australia/wollongong/historic?month=7&year=2018 (accessed Jul. 22, 2020).

[23] T. E. Hoff, R. Perez, J. Kleissl, D. Renne, and J. Stein, 'Reporting of irradiance modeling relative prediction errors', *Prog. Photovolt. Res. Appl.*, vol. 21, no. 7, pp. 1514–1519, Nov. 2013, doi: 10.1002/pip.2225.

[24] Jan Kleissl, *Solar Energy Forecasting and Resource Assessment*. Academic Press, 2013.